

1
2
3
4

Rapid basal channel growth beneath Greenland's longest floating ice shelf

Ash Narkevic¹, Bea Csatho¹, Toni Schenk¹

¹Department of Geological Sciences, University at Buffalo, Buffalo, NY, USA.

Corresponding author: A. Narkevic, davidnar@buffalo.edu

Abstract

Nioghalvfjærdsfjorden Glacier (N79) is one of the two main outlets for Greenland's largest ice stream, the Northeast Greenland Ice Stream (NEGIS), and is the more stable of the two, with no calving front retreat expected in the near future. Using a novel elevation reconstruction approach combining digital elevation models (DEMs) and laser altimetry, previously undetected local phenomena are identified complicating this assessment. N79 is found to have a complex network of basal channels that were largely stable between 1978 and 2012. Since then, an along-flow central basal channel has been growing rapidly, likely due to increased runoff and ocean temperatures, and possibly threatening to decouple the glacier's northwestern and southeastern halves.

1 Introduction

The Northeast Greenland Ice Stream (NEGIS) is the largest ice stream of the Greenland Ice Sheet, draining approximately 12% of its surface area and containing a sea-level rise equivalent of 1.1 m (Mouginot et al., 2015). Its discharge is routed through two major outlet glaciers, Zachariæ Isstrøm (ZI) and Nioghalvfjærdsfjorden Glacier (N79) (Fig. 1), the former of which has demonstrated a pattern of accelerating mass loss in recent decades (Mouginot et al., 2019a). N79 features a ~ 70 km long floating ice tongue which provides a substantial buttressing effect to this branch of the ice stream (Mayer et al., 2018). At the end of its containing fjord, the ice tongue terminates upon a sill (Morlighem et al., 2017; An et al., 2021).

N79 experienced only minor changes in calving front and grounding line position between 1978 and 2020 (Fig. 1A, Supporting Information Fig. S1), possibly as a result of this configuration. Moreover, models such as the Ice Sheet Systems Model (ISSM) suggest that its grounding line and calving front are unlikely to change significantly over the next century (Choi et al., 2017). However, cosmogenic exposure and radiocarbon dating of surrounding rocks indicate that both N79 and ZI have retreated well inland from their current extents during the Holocene (Larsen et al., 2018), indicating that N79 may be more sensitive to climate change than previously thought. Indeed, velocity measurements show that, while not as dramatically as ZI, N79 has accelerated noticeably in the vicinity of its grounding line ($\sim 10\%$) in recent decades (Mouginot et al., 2015). Moreover, the average water temperature is increasing, and the depth to the upper interface of warm Atlantic Intermediate Water (AIW) is decreasing in the open sea beyond the calving front (Schaffer et al., 2020); and many other glaciers in northern Greenland saw an onset of widespread calving events over the last decade (Ochwat et al., 2022). More recently, evidence of warm AIW has even been found in a marginal surface lake near the N79 grounding line (Bentley et al., 2022).

Laser altimetry time series indicate a dynamic thinning of less than 0.5 m annually between 1999 and 2009 on N79 (Csatho et al., 2014), with longer time series revealing an increased rate of thinning since 2012, with total thinning reaching over 50 m by 2020 close to the grounding line near the center of the glacier (Narkevic et al., 2020). However, this is only observed in a few locations because the sparse spatial coverage of airborne laser altimetry between 2009-2018 (Supporting Information Fig. S2) obscured whether the effect was a minor localized phenomenon or a more widespread trend that largely evaded the available altimetry flight lines. This question has significant implications, as reconstructions based on altimetry (e.g., Khan et al., 2022) make broad conclusions about N79 and other glaciers based on these sparse data.

This uncertainty can be mitigated by including digital elevation models (DEMs), which have a much denser spatial distribution of elevation data, albeit at the cost of poorer precision than altimetry. Using altimetry as control data for correcting any systematic error present in DEMs from multiple years within the time frame of interest can produce

55 a reconstruction with high spatiotemporal resolution and accuracy. Here we present a
56 novel elevation reconstruction of the N79 grounding region using such a technique.

57 2 Methods

58 Repeat coverage of WorldView (WV) stereo satellite imagery since 2011 enables
59 the determination of ice sheet elevation changes with high spatial resolution and accu-
60 racy (Porter et al., 2022; Shean et al., 2019). We used ArcticDEM strips, generated from
61 WV images using the Surface Extraction with TIN-based Search-space Minimization (SETSM)
62 approach (Noh & Howat, 2018), to reconstruct elevation changes in the N79 region be-
63 tween 2012-2020. These DEMs, calculated using satellite ephemeris information only with-
64 out applying ground control, still have vertical errors on the order of 4 m (Porter et al.,
65 2022), which is unsuitable for precise change detection and investigating ice dynamic pro-
66 cesses of outlet glaciers. We developed a correction algorithm, based on the approach
67 of Schenk et al. (2014) to reduce this error. Altimetry time series, serving as control, were
68 generated from Operation IceBridge Airborne Topographic Mapper (ATM) airborne (1993-
69 2019), ICESat (2003-2009) and ICESat-2 (2018-present) satellite data using the Surface
70 Elevation Reconstruction and Change Detection (SERAC) method (Schenk & Csatho,
71 2012). A spline-based approximation algorithm (Shekhar et al., 2021) infers the eleva-
72 tion at the date of the DEM acquisition for each time series, and a third-order polyno-
73 mial correction surface is fitted to the resulting residuals for a given DEM. Once added
74 to the DEM, the error is reduced, and separate DEMs can be mosaicked together with
75 minimal edge discontinuity and a final uncertainty on the order of ~ 1 m (Supporting In-
76 formation Text S1). The pipeline also accounts for tidal flexure and the inverse baro-
77 metric effect on floating ice (Supporting Information Text S2). In this manner, ice sur-
78 face elevation DEMs, covering the N79 grounding line region, are created for 2012, 2014-
79 2017, and 2020, with nominal dates in the spring to early summer (Supporting Informa-
80 tion Table S1). The Greenland Ice Mapping Project (Howat et al., 2014) surface DEM
81 is used outside the spatial extent of the corrected DEMs. A DEM generated from 1978
82 stereo aerial photographs (Korsgaard et al., 2016) is used for determining long-term el-
83 evation changes. Landsat and Sentinel imagery is used for qualitative assessment of sur-
84 face features (e.g., Supporting Information Table S2).

85 The 2012-2020 gridded surface elevation reconstructions form the basis of several
86 other data sets. Eulerian (static reference frame) annual elevation change is calculated
87 as the direct difference between surface heights for consecutive years. Furthermore, us-
88 ing a hydrostatic assumption and a bathymetry model from An et al. (2021) as the bed
89 elevation, the depth to the bottom of the ice shelf was inferred for each year and also
90 used for estimating grounding line location (Supporting Information Text S3). The ac-
91 curacy of the derived ice bottom elevations is assessed by comparing them with airborne
92 ice-penetrating radar (IPR) returns (CRISIS, 2020). Basal drainage patterns are inferred
93 for each year from the surface and bed DEMs using the MatLab Topo Toolbox (Schwanghart
94 & Nikolaus, 2010), and tested for robustness using a Monte Carlo analysis as described
95 in Narkevic (2021). Using this reconstructed basal routing to demarcate a basal drainage
96 basin for N79, annual aggregate runoff is estimated using values from the Regional At-
97 mospheric Climate Model v2.3p2 (van Wessem et al., 2018), assuming all runoff reaches
98 the bed immediately.

99 Velocities for the period of interest, derived from a combination of radar and opti-
100 cal images using feature tracking and interferometry, are from Mouginot et al. (2019b).
101 These are summer-to-spring annual averages from 2012-2017. From these, the surface
102 strain rate components are derived and used as a proxy for surface stresses, and have
103 an estimated uncertainty of ~ 0.01 yr⁻¹ based on the uncertainty in velocity. Eulerian
104 change rates on floating ice are complicated by the advection of large fractures, so the
105 velocities are used to reconstruct Lagrangian (moving reference frame) elevation changes
106 for this region, i.e., taking the difference between elevation at an initial pixel, and the

pixel to which that ice parcel would have advected by the subsequent DEM date (Supporting Information Text S4). This is performed in the manner of Shean et al. (2019).

Finally, to investigate the propagation of dynamic thinning to the grounded ice, SERAC time series derived from altimetry were partitioned into components due to surface processes as estimated by the IMAU-FDM v1.2G model (Brils et al., 2022) and ice dynamics.

3 Results

The cause of the anomalous rapid thinning detected by some SERAC time series is immediately apparent when comparing reconstructions from different years: a large along-flow channel appears in the center of the ice shelf near the grounding line, which experiences a higher rate of thinning than the surrounding ice (Fig. 1B and D-F). Moreover, it is not a novel feature of the ice, but part of an existing pattern of channels that has become increasingly exaggerated over time.

3.1 Morphology of N79

The floating ice shelf of N79 exhibits a lateral dichotomy. The northwestern ice shelf (NWIS) gradually becomes thinner with distance from the grounding line and is marked by a relatively uniform pattern of crevasses, while the southeastern ice shelf (SEIS) is characterized by larger, sparser flow-perpendicular channels separated by ~ 5 -10 km with surface bulges in between (Figs. 1B, 2A). The bulges create an across-flow step-wise thickness discontinuity up to ~ 100 m at the center of the floating tongue (Reeh et al., 2000, Fig. 1C). This pattern remains visible within ~ 40 km of the grounding line, beyond which the two halves appear more uniform. There are also three major along-flow channels, one at each margin, and one in the center. The central channel is less uniform than the others, consisting of segments trailing upstream from the northwest end of the SEIS flow-perpendicular channels. Around 2000, a second band of channels with a more oblique orientation appeared closer to the margin, essentially on top of the SEIS marginal channel (Fig. 1B yellow features), one of which causes the southern channel to fork (i.e., Figs. 1C, 1E). Overall, between 1978 and 2020, the ice sheet has become thinner, with more intense and complex channelization, with several channels reaching the grounding line by 2020 (Figs. 1D-F, Supporting Information Figs. S1B, S5).

The flow-perpendicular channels in SEIS are not necessarily analogous to the crevasses in NWIS. Near the grounding line, one can observe annual "ripples" in the ice sheet that first appear angled upstream toward the center and are reminiscent of the basal channel pattern predicted for heterogeneous ice tongues under no-slip conditions by Sergienko (2013), and may represent the nascent form of the large flow-perpendicular channels. These generally rotate until perpendicular to flow, and some ultimately grow a new segment of the central channel, forming a hook shape, and developing a complex surface morphology with internal ridges (Fig. 2B). If in hydrostatic equilibrium, these ridges would correspond to subglacial keels, or they may be uncompensated compressional features. There are no radar flights spanning the flow-perpendicular channels to indicate which is the case. Over time (i.e., with distance from the grounding line), the flow-perpendicular channels tend to become narrower along-flow and more subdued in vertical relief.

Around 2012, two flow-perpendicular channels emerged near the grounding line in close proximity, the second of which did not fully rotate into flow-perpendicular position in subsequent years (Fig. 1B). The central channel segment connected to this flow-perpendicular channel has since grown, thinning the ice in its location at a prodigious rate, reaching nearly 100 myr^{-1} between 2017-2020 at the intersection of the transects in Figs. 2C-2D. This thinning is nearly twice the 50 myr^{-1} melt rate detected in 2011-2015 near the grounding line (Wilson et al., 2017). SERAC time series indicate the ef-

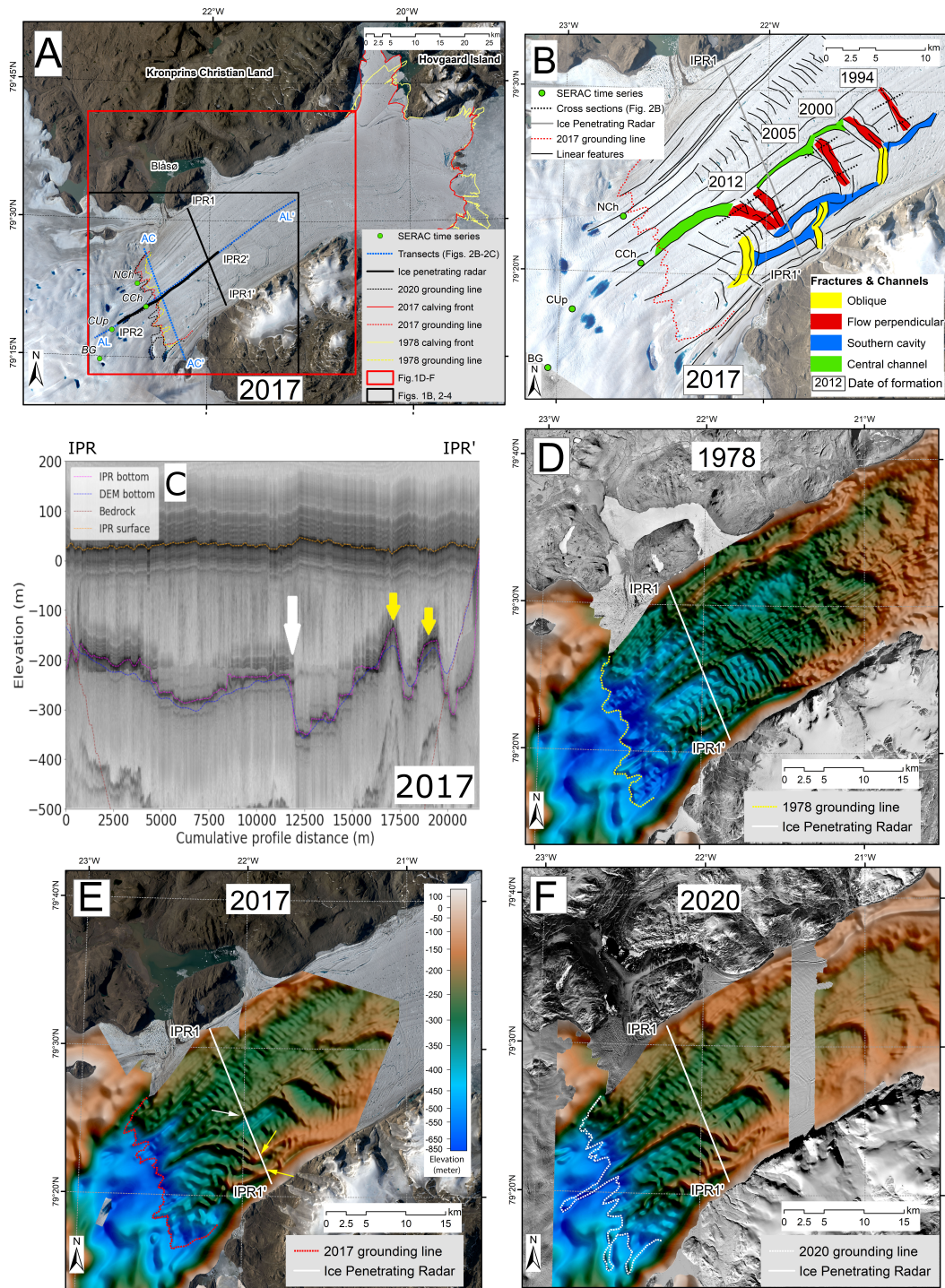


Figure 1. (A) Map of the study area showing calving-front and grounding-line changes between 1978 and 2020, and the locations of transects and SERAC time series. The larger box marks the area shown in Figs. 1D-1E, and the smaller box in Figs. 1B, 2-4, and Supporting Information Figs. S5-7. (B) Interpretation of observable surface features, with the year of formation for flow-perpendicular channels. (C) IPR profile from April 3, 2017, showing the abrupt flow-perpendicular thickness change across the center (white arrow) and the (forked) southeast marginal channel (yellow arrows, see arrows also in Fig. 1E). (D) 1978 ice bottom reconstruction, showing the buoyancy-inferred bottom depth for floating ice, and bedrock depth elsewhere. (E, F) Similar reconstructions for 2017 and 2020. Satellite images and aerial photographs shown in the figures are listed in Supporting Information Table S2.

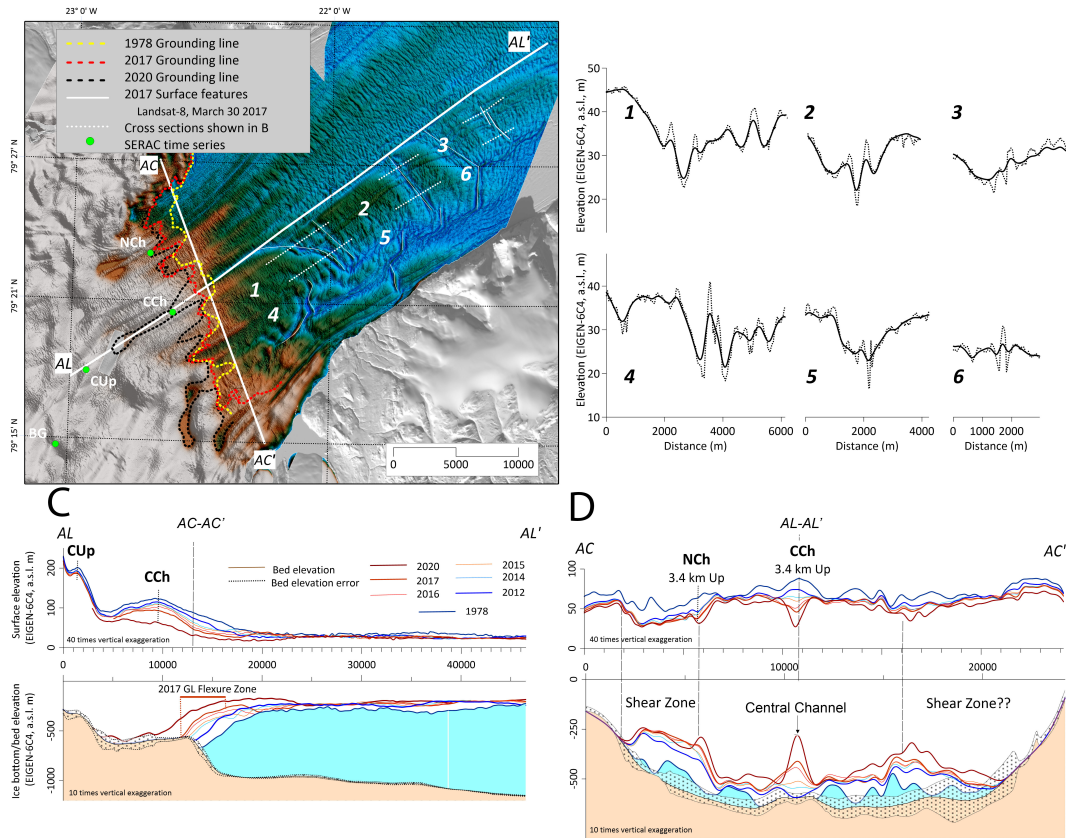


Figure 2. (A) Shaded relief ice surface elevation in 2017 with grounding line locations, ice shelf fractures from Landsat imagery, and locations of transects shown B. (B) Surface elevation profiles across flow-perpendicular channels, illustrating their complex morphology. Dotted lines show elevations from the 30-meter resolution DEM and solid lines from the DEM smoothed by a Gaussian kernel of 600 meter to emphasize surface topography reflecting basal channels. (C) Along and (D) Across-flow profiles of ice surface and bottom elevation showing central channel growth (C, D), grounding line retreat (C), and thinning in the shear zones (D). Shear zone extent is defined based on across-flow strain rates (Fig. 4B) and 2017 grounding line flexure zone is from (ESA, 2017)

156 facts were already detectable upstream of the grounding line by ~ 2015 (Fig. 3F). Thin-
 157 ning continued along the basal channel and the connected subglacial channel (Figs. 3F,
 158 S6), and by 2020 the hydrostatically-inferred grounding line had experienced significant
 159 local retreat upstream of the central and SEIS marginal channels (Figs. 2A, 2C). This
 160 effect was sufficiently pronounced to shift the basal drainage patterns in the area. The
 161 potential basal drainage pathways from the reconstruction indicate three major outlets
 162 into the fjord: two corresponding to the marginal channels and one that, before 2016,
 163 entered the fjord about 1 km southeast of the central channel. By 2016 the channelized
 164 thinning shifted this pathway directly into the central channel (Fig. 3A, Supporting In-
 165 formation Fig. S5). The ensuing inferred grounding line retreat then proceeded along
 166 the central and southern basal drainage paths. These results, however, come with the
 167 caveat that the bed elevation in this area is uncertain and cannot be strongly claimed
 168 without additional evidence described below.

169 While there are no radar flights over the basal channel-subglacial channel system,
 170 inferences supporting its rapid thinning and corresponding grounding line retreat can
 171 be made from the 2014 and 2017 along-flow IPR transects, which are slightly southeast
 172 of and parallel to the channel (Fig. 3B-C). In the grounding zone (7500 to 13000 m along-
 173 track) one can see that the ice bottom horizon by 2017 has become both more reflective,
 174 indicating there is more water, and slightly higher. This suggests the area was grounded
 175 in 2014, and not fully grounded three years later. The ice bottom derived from surface
 176 elevation assuming hydrostatic equilibrium underestimates the bottom of the floating
 177 ice (Fig. 3C), suggesting that the ice is not in hydrostatic equilibrium. The 2017 radar
 178 profile also depicts the rapidly thinning ice shelf basal channel as a new "ghost" hori-
 179 zon ~ 200 m above the ice bottom picks, which is likely a side echo from the bottom of
 180 the basal channel, about 100 m higher than it was in 2014 (Fig. 3B, 3C). One can also
 181 see the expression of the basal channel at the point where the flight crosses the hook-
 182 shaped connection between the central and 2012 flow-perpendicular channels, and it is
 183 even thinner than in the surface DEM-based reconstruction. Finally, the flattening of
 184 the ice sheet surface "bump" along the basal channel by 2020 (Fig. 2C, around CCh) also
 185 suggests the transition from grounded ice to floating ice conditions.

186 The increasing dynamic thinning of the grounded ice is illustrated by the SERAC
 187 elevation time series reconstructions shown in Fig. 3F. About 2.5 km upstream of the
 188 2015-2017 grounding line over the subglacial channel connecting to the central channel,
 189 there is a sudden ten-fold increase in the rate of surface thinning beginning around 2015
 190 (CCh) and a three-fold increase as far as ~ 7 km upstream of the grounding line (CUp)
 191 by the following year. It appears this onset of thinning may be unique to the central chan-
 192 nel, as there is no similar pattern upstream of the grounding line along the northern sub-
 193 glacial drainage route (NCh; there is insufficient data to construct an elevation time se-
 194 ries along the southern drainage route), nor is there any detectable change in the rate
 195 of thinning at a typical "background" point (BG).

196 **3.2 Dynamics of N79**

197 The NW-SE lateral dichotomy may be due to rheological heterogeneity in the ice
 198 tongue. N79 contains both ice from NEGIS, which originates in a region of elevated geother-
 199 mal heat (Rogozhina et al., 2016), and from a tributary that merges from the west very
 200 near the outlet, which is likely to be colder and less plastic. Thus, stress may be more
 201 prone to build up in SEIS, being accommodated more sporadically and explosively than
 202 in NWIS. The inferred surface strain rates (Figs. 4, S7) seem to confirm this. Entering
 203 the confines of the fjord imposes along-flow compressive strain on the ice tongue. In NWIS,
 204 the compression is fairly uniform, but in SEIS it is specifically concentrated along the
 205 flow-perpendicular channels, perhaps explaining their complex morphology and narrow-
 206 ing over time. More worrisome is the fact that shear strain has recently manifested along
 207 the central channel, suggesting the NWIS and SEIS halves of the ice tongue may be de-

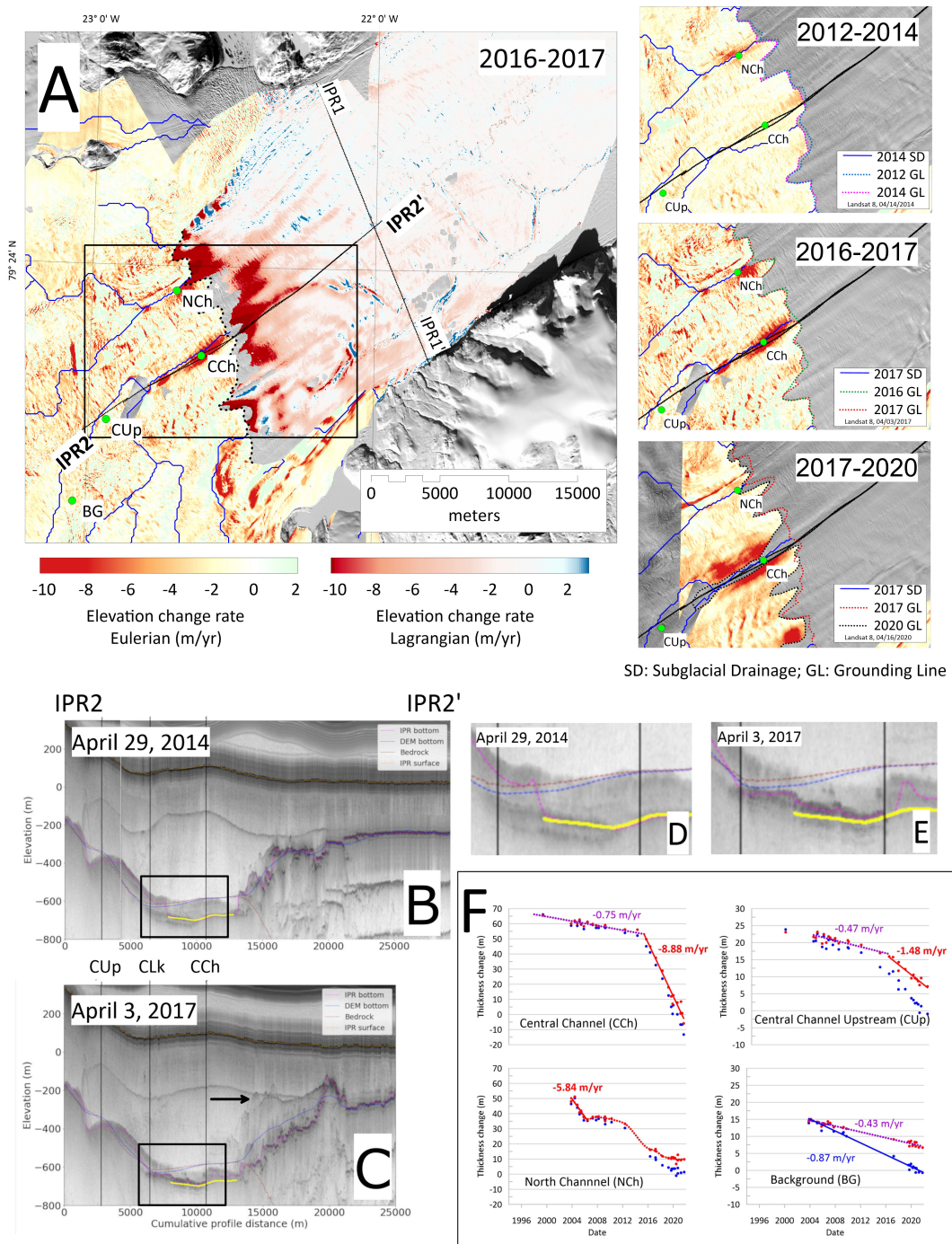


Figure 3. (A) Surface elevation change rate from 2016-17 showing the Eulerian difference on grounded ice and the Lagrangian difference on floating ice, with inferred major subglacial hydrologic pathways. Small maps on the right show the Eulerian annual elevation change rates near the grounding line for 2012-2014, 2016-2017, and 2017-2020. (B) Along-flow radar returns near the center line from 2014. (C) Radar returns from the same flight path on April 3, 2017. Note the thinning and increase in reflectivity (over the yellow line marking the 2014 ice bottom), and the side echo indicated by a black arrow. (D-G) Time series of elevation change for selected locations on grounded ice (green-filled circles in Fig. 3A). Total elevation change is shown in blue, and the dynamic component in red.

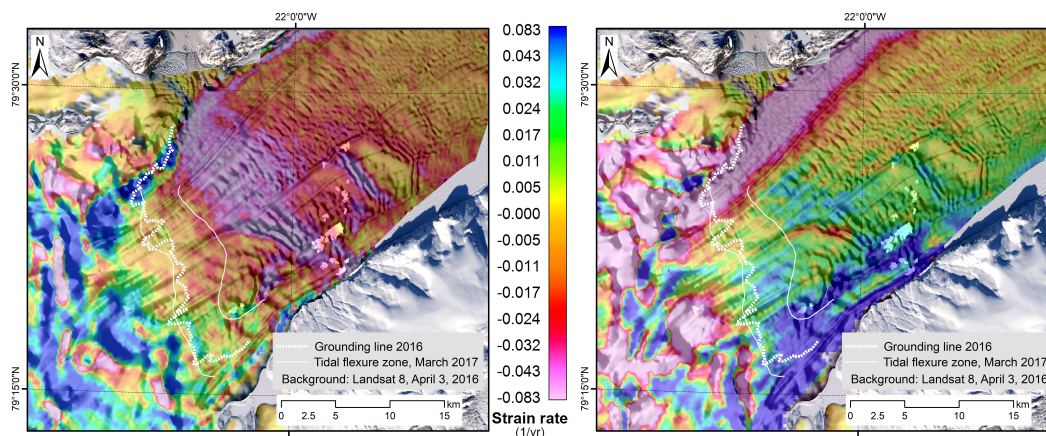


Figure 4. (A) Along-flow strain rate component inferred from the yearly average velocity 2016-17. (B) The corresponding shear strain rate component.

208 coupling as the channel becomes more incised. What effects this could have on the ice
 209 sheet’s stability are not immediately obvious.

210 Yet, this regime of stress distribution and channel formation has existed since at
 211 least 1978 and does not appear to have caused thinning of this magnitude in the mid-
 212 dle of the ice shelf until recently. The likely causes of this severe localized thinning are
 213 several-fold. It is probable that infiltration of warm AIW has increased, leading to more
 214 intense meltwater plume activity at the ice-ocean interface. Runoff rates have also contin-
 215 ued to rise over the past few decades (Fig. S9), with 2012, when the most recent flow-
 216 perpendicular channel formed, being a year of particularly intense melting (Nghiem et
 217 al., 2012), with significant calving events across northern Greenland (Ochwat et al., 2022).
 218 Moreover, the non-perpendicular angle of the attached flow-perpendicular channel and
 219 the shift in basal drainage patterns could make the central channel a particularly conduc-
 220 tive conduit for housing an active meltwater plume

221 4 Conclusion

222 Despite its complicated system of subglacial channels, we find that N79 was rel-
 223 atively stable for many years (at least from 1978-2012). A flow-perpendicular channel/central
 224 channel complex would appear and grow modestly for 5-10 years, but that growth would
 225 significantly diminish when a new flow-perpendicular channel appears and the old one
 226 begins to stagnate. One might liken this to the configuration of Jakobshavn Glacier prior
 227 to the disintegration of its floating icetongue in 1998 (Thomas et al., 2003). Like N79,
 228 Jakobshavn is sourced from two tributaries and had a large basal channel near the ground-
 229 ing line along the seam between these two branches. This channel began to grow, likely
 230 as a result of thickening of the warm water layer at the bottom of the fjord (Motyka et
 231 al., 2011). However, disintegration did not occur until the channel drew close to the calv-
 232 ing front, and for the central channel of N79 this is decades away. There is also a resem-
 233 blance to recent events at Petermann Glacier, which has a similarly long ice shelf, where
 234 grounding line retreat has been facilitated by rising ocean temperature (Washam et al.,
 235 2019) and fractures causing sections of the ice to become decoupled from one another
 236 (Millan et al., 2022).

237 While the impact of these developments on the ice sheet may not be felt for many
 238 years, there are still several insights to be gained. Firstly, the importance of continued
 239 high-density data collection must be stressed. Such observations cannot be made with-

240 out a high spatiotemporal density of altimetry, DEMs, and surface velocities. Ideally,
241 there would also be a greater density of radar observations, as there are presently no more
242 effective methods of determining the true shape of the ice shelf bottom, and the avail-
243 able data was insufficient to meet the full needs of this research. Furthermore, the ob-
244 served changes occur so quickly and are so localized that they would be very difficult to
245 detect without processing such as that described here of combining datasets to improve
246 their collective accuracy.

247 Perhaps more significantly, the results also hint at the weaknesses of our current
248 fundamental ability to model ice sheets. The channels of N79 and their varied behav-
249 ior are too small-scale and temporally variable to be easily incorporated in a model, yet
250 the effects are rather dramatic. Simply turning up the ocean temperature beneath a gen-
251 eralized model of the N79 ice shelf is unlikely to result in the shelf being nearly split in
252 two so close to the grounding line; and generalizing from localized data could be mis-
253 leading. Consider Mayer et al. (2018), which reconstructs the mass loss of N79 largely
254 based on observations of a single feature near the NWIS margin. We conclude that such
255 an approach is misleading, given the non-uniformity in the pattern of thinning of N79.
256 It is our hope that other researchers will continue to strive for greater density and ac-
257 curacy of data, and increased model complexity. The tools developed for this research,
258 once made publicly available, should assist in this regard, as they allow for more accu-
259 rate elevation reconstruction of floating ice, and areas where adequate ice-free control
260 surfaces are unavailable.

261 5 Open Research

262 The software used to generate the elevation reconstructions is the Mosaic Utility
263 and Large Dataset Integration for SERAC (MOULINS) (Narkevic, 2021), which is still
264 in development for public release. It includes spline-based curve fitting based on (Shekhar
265 et al., 2021), and tidal correction based on software available at ([https://github.com/
266 tsutterley/pyTMD](https://github.com/tsutterley/pyTMD)). The altimetry data used come from the Airborne Topographic Map-
267 per (ATM; <https://nsidc.org/data/ilatm2/versions/2>), ICESat ([https://nsidc
268 .org/data/glah12/versions/34](https://nsidc.org/data/glah12/versions/34)), and ICESat-2 ([https://nsidc.org/data/at106/
269 versions/4](https://nsidc.org/data/at106/versions/4)). Uncorrected DEMs from 2012-2020, generated from WorldView imagery
270 by the ArcticDEM project and are available at [https://data.pgc.umn.edu/elev/dem/
271 setsm/ArcticDEM/strips/s2s041/2m](https://data.pgc.umn.edu/elev/dem/setsm/ArcticDEM/strips/s2s041/2m)). The 1978 DEM is from [https://www.ncei.noaa
272 .gov/access/metadata/landing-page/bin/iso?id=gov.noaa.nodc:0145405](https://www.ncei.noaa.gov/access/metadata/landing-page/bin/iso?id=gov.noaa.nodc:0145405). Surface
273 elevations outside the reconstructed region are from BedMachine v4 (Morlighem et al.,
274 2017), available at <https://nsidc.org/data/idbmg4/versions/4>, and the bed eleva-
275 tion is from (An et al., 2021), available [https://datadryad.org/stash/dataset/doi:
276 10.7280/D19987](https://datadryad.org/stash/dataset/doi:10.7280/D19987). Subglacial drainage reconstructions are made with Topo Toolbox (Schwanghart
277 & Nikolaus, 2010), available at <https://topotoolbox.wordpress.com/>. The velocities
278 used can be found at <https://datadryad.org/stash/dataset/doi:10.7280/D11H3X>.
279 N79 calving fronts are from (Goliber et al., 2022) and available at from [https://doi.org/
280 10.5281/zenodo.6557981](https://doi.org/10.5281/zenodo.6557981). All Landsat imagery is courtesy of USGS and obtained from
281 <https://earthexplorer.usgs.gov/>. All new data sets generated by this study (sur-
282 face elevation mosaics, corresponding ice bottom elevation, Lagrangian elevation change,
283 and select partitioned time series), are accessible through Zenodo [https://doi.org/
284 10.5281/zenodo.7518206](https://doi.org/10.5281/zenodo.7518206).

285 Acknowledgments

286 The authors wish to thank Laurie Padman and Susan L. Howard for assistance with tidal
287 corrections, and Cornelis van der Veen for helpful discussion. This research was made
288 possible with the following funding: NASA Sea-Level Change Team (Grant 80NSSC17K0611),
289 ICESat-2 Science Team (Grant 80NSSC21K0915), and NSF Polar and Cyberinfrastruc-
290 ture programs (Grant OAC-2004826).

References

- An, L., Rignot, E., Wood, M., Willis, J., Mouginot, J., & Khan, S. (2021). Ocean melting of the Zachariae Isstrøm and Nioghalvfjærdsfjorden glaciers, northeast Greenland. *Proceedings of the National Academy of Sciences*, *118*(2). doi: 10.1073/pnas.2015483118
- Bentley, M., Smith, J., Jamieson, S., Lindeman, M., Rea, B., Humbert, A., . . . Roberts, D. (2022). Direct measurement of warm Atlantic Intermediate Water close to the grounding line of Nioghalvfjærdsfjorden (79N) Glacier, North-east Greenland. *The Cryosphere Discussions*, *2022*, 1–25. doi: 10.5194/tc-2022-206
- Brils, M., Kuipers Munneke, P., van de Berg, W. J., & van den Broeke, M. (2022). Improved representation of the contemporary Greenland ice sheet firn layer by IMAU-FDM v1.2G. *Geoscientific Model Development*, *15*(18), 7121–7138. doi: 10.5194/gmd-15-7121-2022
- Choi, Y., Morlighem, M., Rignot, E., Mouginot, J., & Wood, M. (2017). Modeling the response of Nioghalvfjærdsfjorden and Zachariae Isstrøm glaciers, Greenland, to ocean forcing over the next century. *Geophysical Research Letters*, *44*(21), 11071–11079. doi: 10.1002/2017gl075174
- CReSIS. (2020). *L1B Geolocated Radar Echo Strength Profile Images Data* [Dataset]. Digital Media. doi: data.cresis.ku.edu/data/rds/
- Csatho, B., Schenk, A., van der Veen, C., Babonis, G., Duncan, K., Rezvanbehbahani, S., . . . van Angelen, J. (2014). Laser altimetry reveals complex pattern of greenland ice sheet dynamics. *Proceedings of the National Academy of Sciences*, *111*(52), 18478–18483. doi: 10.1073/pnas.1411680112
- ESA. (2017). *ESA Greenland Icesheet CCI, Grounding Lines from SAR Interferometry* [Dataset].
- Goliber, S., Black, T., Catania, G., Lea, J. M., Olsen, H., Cheng, D., . . . Zhang, E. (2022). TermPicks: a century of Greenland glacier terminus data for use in scientific and machine learning applications. *The Cryosphere*, *16*(8), 3215–3233. doi: 10.5194/tc-16-3215-2022
- Howat, I., Negrete, A., & Smith, B. (2014). The Greenland Ice Mapping Project (GIMP) land classification and surface elevation data sets. *The Cryosphere*, *8*(4), 1509–1518. doi: 10.5194/tc-8-1509-2014
- Khan, S., Choi, Y., Morlighem, M., Rignot, E., Helm, V., Humbert, A., . . . Bjørk, A. (2022). Extensive inland thinning and speed-up of Northeast Greenland Ice Stream. *Nature*, *611*, 727–732. doi: 10.1038/s41586-022-05301-z
- Korsgaard, N., Nuth, C., Khan, S., Kjeldsen, K., Bjørk, A., Schomacker, A., & Kjær, K. (2016). Digital elevation model and orthophotographs of Greenland based on aerial photographs from 1978–1987. *Scientific Data*, *3*(1), 160032. doi: 10.1038/sdata.2016.32
- Larsen, N., Levy, L., Carlson, A., Buizert, C., Olsen, J., Strunk, A., . . . Skov, D. (2018). Instability of the Northeast Greenland Ice Stream over the last 45,000 years. *Nature Communications*, *9*(1), 1–8. doi: 10.1038/s41467-018-04312-7
- Mayer, C., Schaffer, J., Hattermann, T., Floricioiu, D., Krieger, L., Dodd, P., . . . Schannwell, C. (2018). Large ice loss variability at Nioghalvfjærdsfjorden Glacier, Northeast-Greenland. *Nature Communications*, *9*(1), 1–11. doi: 10.1038/s41467-018-05180-x
- Millan, R., Mouginot, J., Derkacheva, A., Rignot, E., Milillo, P., Ciraci, E., . . . Bjørk, A. (2022). Ongoing grounding line retreat and fracturing initiated at the Petermann Glacier ice shelf, Greenland, after 2016. *The Cryosphere*, *16*(7), 3021–3031. doi: 10.5194/tc-16-3021-2022
- Morlighem, M., Williams, C., Rignot, E., An, L., Arndt, J., Bamber, J., . . . Zinglarsen, K. (2017). BedMachine v3: Complete bed topography and ocean bathymetry mapping of Greenland from multibeam echo sounding combined with mass conservation. *Geophysical Research Letters*, *44*(21), 11,051–11,061.

- doi: 10.1002/2017GL074954
- 346 Motyka, R., Truffer, M., Fahnestock, M., Mortensen, J., Rysgaard, S., & Howat, I.
347 (2011). Submarine melting of the 1985 Jakobshavn Isbræ floating tongue and
348 the triggering of the current retreat. *Journal of Geophysical Research: Earth*
349 *Surface*, 116(F1). doi: 10.1029/2009JF001632
- 350 Mouginit, J., Rignot, E., Bjørk, A., van den Broeke, M., Millan, R., Morlighem, M.,
351 ... Wood, M. (2019a). Forty-six years of greenland ice sheet mass balance
352 from 1972 to 2018. *Proceedings of the National Academy of Sciences*, 116(19),
353 9239-9244. doi: 10.1073/pnas.1904242116
- 354 Mouginit, J., Rignot, E., Scheuchl, B., Fenty, I., Khazendar, A., Morlighem, M.,
355 ... Paden, J. (2015). Fast retreat of Zachariæ Isstrøm, northeast Greenland.
356 *Science*, 350(6266), 1357-1361. doi: 10.1126/science.aac7111
- 357 Mouginit, J., Rignot, E., Scheuchl, B., Wood, M., & Millan, R. (2019b). *Annual ice*
358 *velocity of the greenland ice sheet (2010-2017)* [Dataset]. UC Irvine. Retrieved
359 from <https://datadryad.org/stash/dataset/doi:10.7280/D11H3X> doi: 10
360 .7280/D11H3X
- 361 Narkevic, D. (2021). *Fusion of altimetry and Digital Elevation Models for*
362 *change detection at the Northeast Greenland Ice Stream* (Doctoral disserta-
363 tion, State University of New York at Buffalo). Retrieved from [https://](https://www.proquest.com/openview/60e1c501f94c1bd5a0b3aa334ccce757/1?pq-origsite=gscholar&cbl=18750&diss=y)
364 [www.proquest.com/openview/60e1c501f94c1bd5a0b3aa334ccce757/](https://www.proquest.com/openview/60e1c501f94c1bd5a0b3aa334ccce757/1?pq-origsite=gscholar&cbl=18750&diss=y)
365 [1?pq-origsite=gscholar&cbl=18750&diss=y](https://www.proquest.com/openview/60e1c501f94c1bd5a0b3aa334ccce757/1?pq-origsite=gscholar&cbl=18750&diss=y)
- 366 Narkevic, D., Csatho, B., & Schenk, T. (2020). Rapid thinning at the grounding line
367 of Northeast Greenland's N79 Glacier revealed by new elevation reconstruc-
368 tion. *Abstract C028-0017, Presented at the 2020 AGU Fall Meetings*.
- 369 Nghiem, S., Hall, D., Mote, T., Tedesco, M., Albert, M., Keegan, K., ... Neumann,
370 G. (2012). The extreme melt across the Greenland ice sheet in 2012. *Geophys-*
371 *ical Research Letters*, 39(20). doi: 10.1029/2012GL053611
- 372 Noh, M.-J., & Howat, I. M. (2018). IceBridge ATM L2 Icessn Elevation, Slope,
373 and Roughness, Version 2 [Greenland]. *Boulder, Colorado USA. NASA*
374 *National Snow and Ice Data Center Distributed Active Archive Center*.
375 Retrieved from <https://doi.org/10.5067/E9E9QSRNLYTK> doi:
376 10.5067/E9E9QSRNLYTK
- 377 Ochwat, N., Scambos, T., Fahnestock, M., & Stammerjohn, S. (2022). Character-
378 istics, recent evolution, and ongoing retreat of Hunt Fjord Ice Shelf, northern
379 Greenland. *Journal of Glaciology*, 1-14. doi: 10.1017/jog.2022.44
- 380 Porter, C., Morin, P., Howat, I., Noh, M., Bates, B., Peterman, K., ... Bojesen, M.
381 (2022). *ArcticDEM – Strips, Version 4.1* [Dataset]. Harvard Dataverse, V1.
382 Retrieved from [https://data.pgc.umn.edu/elev/dem/setsm/ArcticDEM/](https://data.pgc.umn.edu/elev/dem/setsm/ArcticDEM/geocell/v3.0/2m)
383 [geocell/v3.0/2m](https://data.pgc.umn.edu/elev/dem/setsm/ArcticDEM/geocell/v3.0/2m) doi: 10.7910/DVN/OHHUKH
- 384 Reeh, N., Mayer, C., Olesen, O., Christensen, E., & Thomsen, H. (2000). Tidal
385 movement of Nioghalvfjærdsfjorden glacier, northeast Greenland: Obser-
386 vations and modelling. *Annals of Glaciology*, 31, 111-117. doi: 10.3189/
387 172756400781820408
- 388 Rogozhina, I., Petrunin, A., Vaughan, A., Steinberger, B., Johnson, J., Kaban, M.,
389 ... Koulakov, I. (2016). Melting at the base of the Greenland ice sheet ex-
390 plained by Iceland hotspot history. *Nature Geoscience*, 9(5), 366-369. doi:
391 10.1038/ngeo2689
- 392 Schaffer, J., Kanzow, T., von Appen, W., von Albedyll, L., Arndt, J., & Roberts, D.
393 (2020). Bathymetry constrains ocean heat supply to Greenland's largest glacier
394 tongue. *Nature Geoscience*, 13(3), 227-231. doi: 10.1038/s41561-019-0529-x
- 395 Schenk, T., & Csatho, B. (2012). A new methodology for detecting ice sheet surface
396 elevation changes from laser altimetry data. *IEEE Transactions on Geoscience*
397 *and Remote Sensing*, 50(9), 3302-3316. doi: 10.1109/TGRS.2011.2182357
- 398 Schenk, T., Csatho, B., Veen, C. V. D., & McCormick, D. (2014, 00). Fusion of
399 multi-sensor surface elevation data for improved characterization of rapidly
400

- 401 changing outlet glaciers in Greenland. *Remote Sensing of Environment*, 149,
402 239 – 251. doi: 10.1016/j.rse.2014.04.005
- 403 Schwanghart, W., & Nikolaus, J. (2010). TopoToolbox: A set of Matlab functions
404 for topographic analysis. *Environmental Modelling & Software*, 25(6), 770-781.
405 doi: 10.1016/j.envsoft.2009.12.002
- 406 Sergienko, O. (2013). Basal channels on ice shelves. *Journal of Geophysical Re-*
407 *search: Earth Surface*, 118(3), 1342-1355. doi: 10.1002/jgrf.20105
- 408 Shean, D., Joughin, I., Dutrieux, P., Smith, B., & Berthier, E. (2019). Ice shelf
409 basal melt rates from a high-resolution digital elevation model (DEM) record
410 for Pine Island Glacier, Antarctica. *The Cryosphere*, 13(10), 2633–2656. doi:
411 doi.org/10.5194/tc-13-2633-2019
- 412 Shekhar, P., Csatho, B., Schenk, A., Roberts, C., & Patra, A. (2021). ALPS: A
413 Unified Framework for Modeling Time Series of Land Ice Changes. *IEEE*
414 *Transaction on Geoscience and Remote Sensing*, 59(8), 6466–6481. doi:
415 10.1109/TGRS.2020.3027190
- 416 Thomas, R., Abdalati, W., Frederick, E., Krabill, W., Manizade, S., & Steffen, K.
417 (2003). Investigation of surface melting and dynamic thinning on Jakob-
418 shavn Isbræ, Greenland. *Journal of Glaciology*, 49(165), 231-239. doi:
419 10.3189/172756503781830764
- 420 van Wessem, J. M., van de Berg, W. J., Noël, B. P. Y., van Meijgaard, E., Amory,
421 C., Birnbaum, G., . . . van den Broeke, M. R. (2018). Modelling the cli-
422 mate and surface mass balance of polar ice sheets using RACMO2 – Part
423 2: Antarctica (1979–2016). *The Cryosphere*, 12(4), 1479–1498. doi:
424 10.5194/tc-12-1479-2018
- 425 Washam, P., Nicholls, K., Münchow, A., & Padman, L. (2019). Summer surface
426 melt thins Petermann Gletscher Ice Shelf by enhancing channelized basal melt.
427 *Journal of Glaciology*, 65(252), 662–674. doi: 10.1017/jog.2019.43
- 428 Wilson, N., Straneo, F., & Heimbach, P. (2017, 00). Satellite-derived submarine
429 melt rates and mass balance (2011–2015) for Greenland’s largest remaining ice
430 tongues. *The Cryosphere*, 11(6), 2773 – 2782. doi: 10.5194/tc-11-2773-2017